Clifford K. Ho
Concentrating Solar Technologies Department,
Sandia National Laboratories,
Albuquerque, NM 87185-1127
e-mail: ckho@sandia.gov

Joshua M. Christian
Concentrating Solar Technologies Department,
Sandia National Laboratories,
Albuquerque, NM 87185-1127

David Romano
Dipartimento Energia,
Polytechnic University of Turin,
Corso Duca degli Abruzzi, 24,
Torino 10129, Italy

Julius Yellowhair
Concentrating Solar Technologies Department,
Sandia National Laboratories,
Albuquerque, NM 87185-1127

Nathan Siegel
Mechanical Engineering Department,
Bucknell University,
701 Moore Avenue,
Lewisburg, PA 17837

Laura Savoldi
Dipartimento Energia,
Polytechnic University of Turin,
Corso Duca degli Abruzzi, 24,
Torino 10129, Italy

Roberto Zanino
Dipartimento Energia,
Polytechnic University of Turin,
Corso Duca degli Abruzzi, 24,
Torino 10129, Italy

Characterization of Particle Flow in a Free-Falling Solar Particle Receiver

Falling particle receivers are being evaluated as an alternative to conventional fluid-based solar receivers to enable higher temperatures and higher efficiency power cycles with direct storage for concentrating solar power (CSP) applications. This paper presents studies of the particle mass flow rate, velocity, particle-curtain opacity and density, and other characteristics of free-falling ceramic particles as a function of different discharge slot apertures. The methods to characterize the particle flow are described, and results are compared to theoretical and numerical models for unheated conditions. Results showed that the particle velocities within the first 2 m of release closely match predictions of free-falling particles without drag due to the significant amount of air entrained within the particle curtain, which reduced drag. The measured particle-curtain thickness (~2 cm) was greater than numerical simulations, likely due to additional convective air currents or particle–particle interactions neglected in the model. The measured and predicted particle volume fraction in the curtain decreased rapidly from a theoretical value of 60% at the release point to less than 10% within 0.5 m of drop distance. Measured particle-curtain opacities (0.5–1) using a new photographic method that can capture the entire particle curtain were shown to match well with discrete measurements from a conventional lux meter. [DOI: 10.1115/1.4035258]

1 Introduction

Falling particle receivers are being evaluated to increase operating temperatures and power cycle efficiencies for concentrating solar power (CSP) applications [1]. In falling particle receivers, small sandlike particles are released through a slot above a cavity receiver, where concentrated sunlight directly irradiates and heats the falling particles. The hot particles are stored and then used to heat the working fluid for the power cycle. Conventional CSP plants that employ thermal storage use molten nitrate salt, which decomposes at temperatures less than 600 °C [2]. The use of particle receivers enables particle temperatures over 1000 °C. Previous studies of particle receivers have considered alternative configurations including free-falling [3,4], centrifugal [5,6], flow in tubes with or without fluidization [7–9], multipass recirculation [1,10], north- or south-facing [11,12], and face-down configurations [13]. This paper focuses on the flow characteristics of free-falling particle receivers with comparison to analytical and numerical models. New methods to characterize the opacity of a particle curtain are also introduced.

Previous particle flow studies for solar receivers have shown that particle flow characteristics (velocity, curtain thickness, solids' volume fraction, and curtain opacity) vary as a function of slot aperture size, mass flow rate, particle size, and external conditions (e.g., wind) [14,15]. The particle flow characteristics can subsequently impact particle heating and receiver thermal efficiency [3,16–19]. In the 1980 s, Hruby et al. [20] performed experiments of a free-falling particle curtain using ~650 μm alumina Norton Master Beads. They evaluated the particle velocity and temperatures of heated particles (up to 500 °C) over a drop distance of ~3 m, but the slot length was only 5–6 cm, so the mass flow rates were less than 0.04 kg/s. Rightley et al. also performed small-scale free-falling particle flow tests in a solar furnace and determined the porosity and extinction coefficient of a particle curtain several centimeters in length for heat transfer modeling and characterization. The current tests reflect larger-scale systems with particle-curtain lengths over 1 m and mass flow rates on the order of several kilograms per second. The current tests are likely to include more air entrainment by the particles than the previous smaller-scale tests, which showed a greater influence of air drag on the particles, especially at higher temperatures.

Contributed by the Solar Energy Division of ASME for publication in the Journal of Solar Energy Engineering: Including Wind Energy and Building Energy Conservation. Manuscript received September 18, 2015; final manuscript received November 8, 2016; published online December 22, 2016. Assoc. Editor: Carlos F. M. Coimbra.

Kim et al. [21] investigated the impact of external wind and different angles of attack on particle flow of spherical ceramic particles. They found that a 45 deg wind angle relative to the aperture normal and particle curtains within ~0.5 m of the aperture produced larger particle losses. Tan et al. [22] and Ho et al. [14,23] performed numerical and experimental evaluations of an air curtain in front of the receiver aperture and its ability to mitigate the impacts of external wind on convective heat losses and particle flow instabilities. Kim et al. [24] experimentally evaluated the particle velocity, curtain thickness, solids' volume fraction, and curtain opacity for a drop distance of ~3 m as a function of particle mass flow. Most of the measurements and comparisons to numerical models were performed using a nominal particle size of 697 μm (CARBO HSP). The current study evaluates multiple particle sizes and includes additional comparisons to analytical solutions for the particle mass flow rate as a function of aperture size.

The objective of this paper is to characterize the particle flow characteristics of a ~1 MW_t falling particle receiver prototype constructed by Sandia National Laboratories to test and evaluate the performance of high-temperature falling particle receiver designs. Figure 1 shows a schematic of the prototype and its major components, which include the top hopper, the receiver (~2 m × 2 m × 2 m), the bottom hopper, and a particle elevator to recirculate the particles from the bottom hopper back to the top hopper. The current studies extend previous particle flow characterization studies for solar particle receivers with larger experimental, additional particle sizes, comparisons to new models, and an introduction to a new method to characterize particle-curtain opacity. Only ambient temperatures (~20 °C) are considered in these tests. At higher temperatures expected in solar thermal receivers (~700 °C or higher), the kinematic viscosity of air is significantly higher (by a factor of 7–8), which reduces the Reynolds number and increases the drag coefficient of the particles in air. Thus, the free-falling particle temperature is expected to be less at higher temperatures as observed by Hruby et al. [20].

2 Particle Properties

The ceramic particles used in the tests were CARBO ACCUCAST ID50. These particles have been shown to have excellent durability under high temperatures and good radiative properties. The particle properties are summarized in Table 1. Additional radiative properties (spectral absorptivity and emissivity) can be

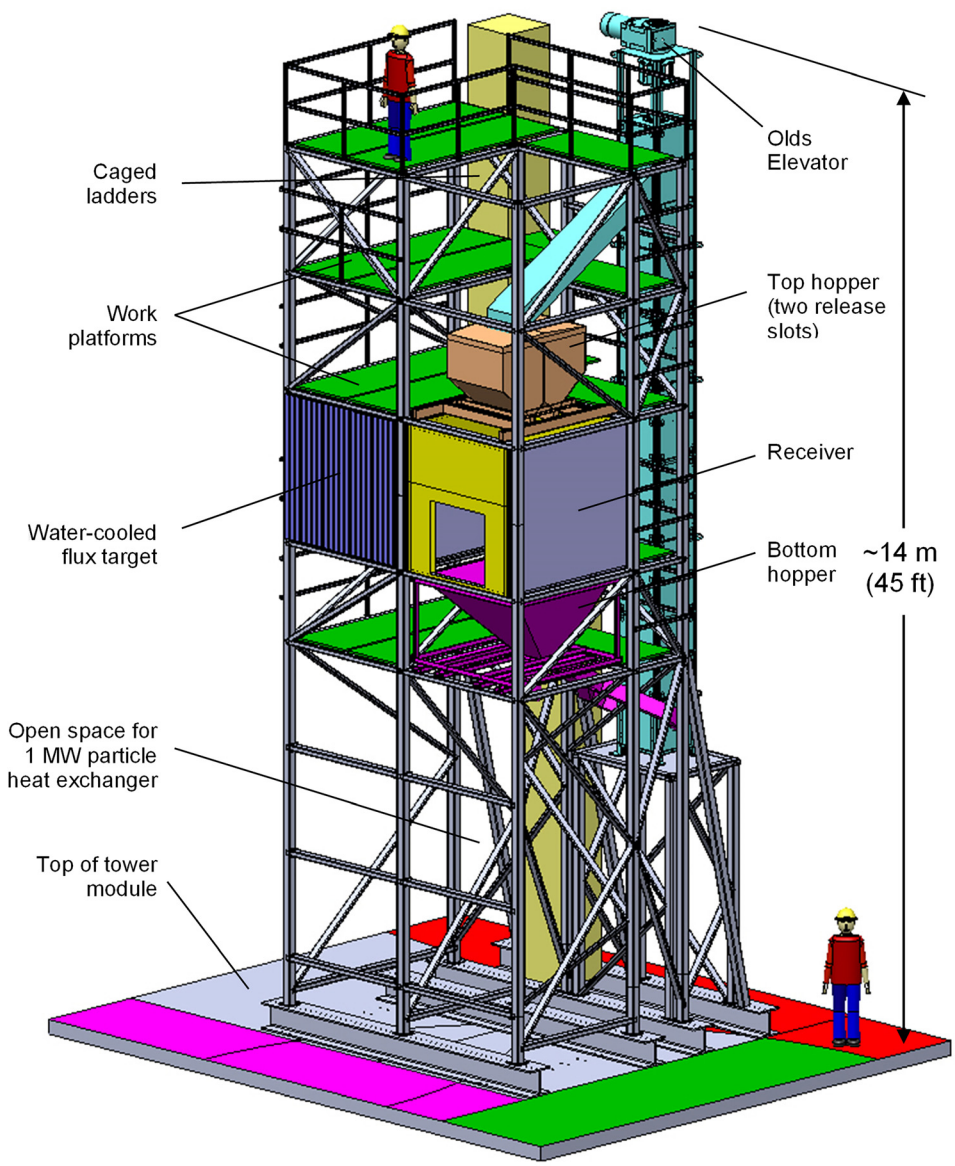

Fig. 1 Falling particle receiver prototype

Table 1 CARBO Accucast ID50 particle properties (from www.carboceramics.com unless otherwise noted)

Property	Value
Mass-median particle diameter (μm)	280
Particle density[a] (kg/m^3)	3300
Loose bulk density at 1100 °C (kg/m^3)	1810
Packed-bed bulk density at 1100 °C (kg/m^3)	2000
Bulk porosity[b]	0.39 (packed) 0.45 (loose)
Packed-bed bulk thermal conductivity at 1100 °C (W/m K)	0.7
Particle thermal conductivity[c] at 1100 °C (W/m K)	2
Specific heat[d] (J/kg K)	$365T^{0.18}$ for 50 °C $\leq T \leq$ 1100 °C
Packed-bed solar absorptance[e]	0.91
Packed-bed thermal emittance[f] at 700 °C	0.75
Sphericity	0.9
Composition	75% Al_2O_3, 11% SiO_2, 9% Fe_2O_3, 3% TiO_2

[a]Measured using Micromeritics AccuPyc 1330 pycnometer (courtesy Andrea Ambrosini, Sandia National Laboratories (SNL)).
[b]Calculated from particle density and loose/packed bulk densities.
[c]Calculated using average of series and parallel bulk thermal conductivity models.
[d]Fit to data from Netzsch STA 409 (courtesy Eric Coker, SNL).
[e]Measured as-received using Surface Optics 410-Solar. See Ref. [25] for degradation at elevated temperatures.
[f]Measured using Surface Optics ET-100 (courtesy James Yuan, SNL).

found in Refs. [25] and [26]. Additional information regarding durability and sintering can be found in Refs. [27] and [28].

3 Particle Mass Flow Rates

3.1 Olds Elevator Mass Flow Rates. The Olds Elevator is used to lift and recirculate particles from the bottom hopper to the top hopper, where the particles are released into the receiver. The elevator procured for Sandia's prototype is rated for operation at ~800 °C. The Olds Elevator employs the Archimedes' screw principle; it has a stationary internal screw and a rotating casing around the screw. The rotating casing scoops particles at the base of the screw and lifts the particles along the flights of the screw via friction. The casing speed is controlled by a variable frequency drive (VFD) connected to a 25 hp motor. The mass flow rate from the elevator is a direct function of the frequency of the VFD. Four frequencies (20, 30, 40, and 54 Hz) were evaluated to establish a reference curve for mass flow rate versus frequency. The particle

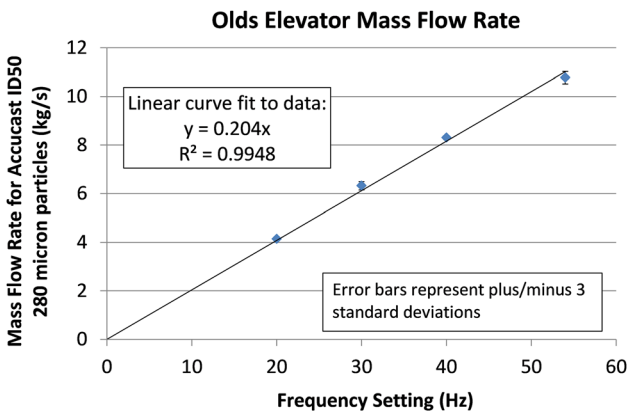

Fig. 2 Measured mass flow rate (kg/s) versus VFD frequency (Hz) in Olds Elevator using CARBO Accucast ID50K ceramic particles with median diameter of 280 μm

Fig. 3 Dimensions (mm) for the 9.53 mm aperture discharge plate

discharge from the top of the Olds Elevator was collected in a hopper suspended by a crane, and a Dillon EDXtreme dynamometer was used to record the mass accumulation as a function of time to determine the mass flow rate. Mass flow measurements at each frequency were repeated three times in random order, and the average mass flow rate for each frequency was plotted in Fig. 2. Results show that the Olds elevator mass flow rate is a linear function of the VFD setting with a coefficient of determination of 0.99.

After the initial elevator mass flow measurements were recorded, the top hopper was assembled, and a longer duct was added to connect the Olds Elevator discharge chute to the top hopper. Discharge plates placed at the base of the top hopper with different slot aperture sizes could then be characterized.

3.2 Mass Flow Rate Through Discharge Plate Slot Apertures. While the Olds Elevator could be used to control the mass flow rate of particles released into the receiver, it would be difficult to evenly distribute the particles falling from the top hopper at varying flow rates. Instead, the prototype design for the top hopper uses discharge plates of fixed slot aperture size. The steel plates are removable so that the mass flow rate of the hopper can be varied by selecting different slot apertures. This system is simple, but it is suitable for high temperatures when moving parts (e.g., slide gates) may pose a problem after thermal expansion. The discharge slot apertures evaluated in this study were 6.35, 9.53, 11.1, and 12.7 mm, which correspond to 1/4, 3/8, 7/16, and 1/2 in., respectively. All slot widths were 1.24 m, and the plate thickness was 4.8 mm (3/16 in.). Figure 3 shows the dimensions of the 9.53 mm (3/8 in.) discharge plate.

If the particle elevator supplies a mass flow rate that exceeds the mass flow rate through the discharge plate, particles will accumulate in the top hopper, and the particles will be released uniformly along the entire length of the discharge slot. Figure 4 shows an example of particles falling through an 11.1 mm slot aperture, producing a well-defined curtain. Secs. 3.2.1 and 3.2.2

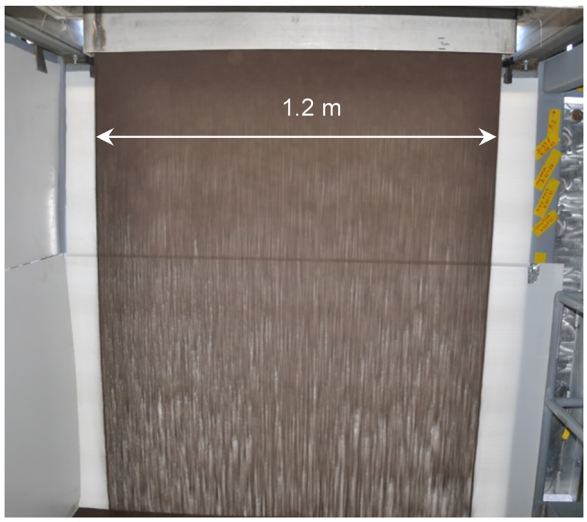

Fig. 4 Falling particle curtain released through 11.1 mm (7/16 in.) discharge slot aperture

describe models and measurements of particle mass flow rates through varying slot aperture sizes.

3.2.1 Modeling Particle Flow Through Apertures. Empirical models have been developed to predict the mass flow rate of granular solids through orifices [29–32]. Janda et al. [31] recommended the following modified form of the Beverloo et al. equation [29]:

$$\dot{m} = C_1 \rho_b \sqrt{g}(D - C_2 d)^{n+0.5} \tag{1}$$

where $\dot{m}$ = mass flow rate (kg/min for 3D or kg/min/m for 2D), C_1 = dimensionless constant related to material properties, ρ_b = bulk density of particles above the aperture (kg/m^3), g = gravitational constant (9.81 m/s^2), D = aperture size (m), C_2 = geometrical factor accounting for the effective outpouring section being smaller than the aperture, d = particle size (m), and n = "1" for 2D and "2" for 3D.

Most of the previous studies using forms of Eq. (1) have focused on agricultural products (e.g., seeds). In Sec. 3.2.2, we attempt to use Eq. (1) for the alumina–silica ceramic particles investigated in this study and determine appropriate dimensionless constants for C_1 and C_2.

3.2.2 Measured Particle Flow Through Apertures. The particle mass flow rate through the different discharge plate slot apertures was measured by setting the Olds Elevator to a high-particle flow rate (greater than the mass flow rate through the slot aperture of the discharge plate in the top hopper). The top hopper accumulated with particles until the entire slot width had a steady flow of particles. The particles that flowed through the aperture were then collected and weighed as a function of time to determine the mass flow rate. The process was repeated for each of the different discharge plates.

Figure 5 shows the results of the measured particle mass flow rates as a function of discharge slot aperture for two different particle sizes. The current study evaluated the 280 μm particles, while the data for the 697 μm particles were obtained from Ref. [3]. The predicted mass flow rates using Eq. (1) are also plotted in Fig. 5 assuming a packed bulk density of 2000 kg/m^3 and fitted values for C_1 and C_2. The particle mass flow rate increases rapidly as the slot aperture increases and decreases as the particle size increases.

The root-sum-squared error between the predicted mass flow rates and the measured mass flow rates as a function of slot aperture size and two different particles sizes was minimized when $C_1 = 62$ and $C_2 = 1.4$. The fit between the data and the model predictions is excellent within the range of the measured values. Thus, Eq. (1) can be used to estimate mass flow rates of ceramic particles as a function of slot aperture and particle size. It is interesting to compare the fitted values of C_1 (62) and C_2 (1.4) for the ceramic particles used in this study with the corresponding values (35 and 1.4, respectively) found in Ref. [29] for agricultural granular solids (e.g., seeds). The difference in C_1 is likely due to the nonspherical shapes investigated by Beverloo, which can lead to differences in friction coefficients and flowability. The ceramic particles used in the current study are quite spherical, which would tend to increase the mass flow as indicated by the higher C_1 constant. As the particles wear due to abrasion, they will retain a spherical shape, and Eq. (1) can still be used with a different particle diameter.

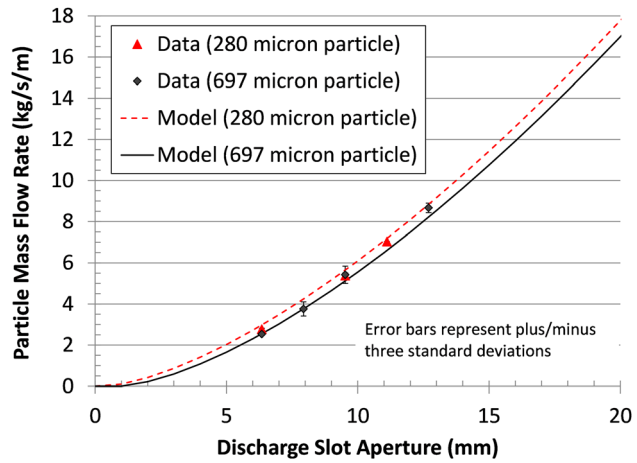

Fig. 5 Measured and modeled mass flow rates as a function of different discharge slot apertures for 280 and 697 μm particle sizes

It should be noted that the maximum mass flow rate of the Olds Elevator was less than the capacity of the 12.7 mm (0.5 in.) slot aperture for 280 μm particles (as evidenced by particles not accumulating in the top hopper nor covering the entire length of the aperture). Therefore, the maximum flow rate shown in Fig. 5 is for the 11.1 mm (7/16 in.) slot aperture.

4 Particle Velocity

4.1 Particle Velocity Modeling. For a particle released from rest, the velocity, v (m/s), as a function of time, t (s), and free-fall distance, y (m), can be expressed as follows by integrating Newton's second law of motion, assuming no drag:

$$v(t) = gt \tag{2}$$

$$v(y) = \sqrt{2gy} \tag{3}$$

If air resistance (drag) is present, the following expressions can be used to determine the velocity as a function of time and position:

$$v(t) = v_\infty \tanh\left(\frac{gt}{v_\infty}\right) \tag{4}$$

$$y(t) = \frac{v_\infty^2}{g} \ln\left(\cosh\left(\frac{gt}{v_\infty}\right)\right) \tag{5}$$

$$v_\infty = \sqrt{\frac{2mg}{\rho_{\text{air}} C_d A}} \tag{6}$$

where v_∞ is the terminal velocity (m/s), m is the mass of the particle (3.79×10^8 kg), ρ_{air} is the air density (1.2 kg/m^3 at 15 °C), A is the cross-sectional area of the particle (6.16×10^8 m^2), and C_d is the coefficient of drag for a sphere (solved iteratively as a function of Reynolds number; $C_d = 2.84$, Re = 36, and $v_\infty = 1.88$ m/s).

Simulations of free-falling particles released through a slot aperture were also performed using ANSYS FLUENT 15.0. The discrete phase model (DPM) was used to simulate particles released from slot apertures of prescribed dimensions corresponding to the test articles. The DPM simulates particle motion in a Lagrangian reference frame governed by a force balance on the particle. The force balance includes a drag force that accounts for the velocity of the particle, velocity of the surrounding fluid, particle size, and fluid properties [33]. The DPM is appropriate for dilute particle flows with solid volume fractions less than ~10%. As shown in Sec. 5, this is a good approximation for most of the particle trajectory. However, near the release point, the solids' volume fraction can be larger than 10%, and particle–particle interaction may be significant, requiring the use of more detailed models (discrete element or dense discrete phase models).

The continuous air phase was simulated with a realizable k–ε turbulence model using the default model constants in FLUENT [34]. A k–ω shear stress transport (SST) turbulence model and a laminar model were also investigated, and the results showed that the difference in particle velocity at the outlet was only ~3%. The velocity at various drop distances was recorded, along with the

particle width, thickness, and concentration. A total of $\sim 1 \times 10^6$ hexahedral elements were used in the model, which consisted of a cubical domain with a slot aperture in the middle of the top surface, walls on the side, and a pressure opening at the bottom. The slot surface consisted of 300×20 elements. A grid independence study using a range of grid resolutions ranging from 64,000 to 4×10^6 hexahedral elements was performed to ensure that the resolution of the grid was sufficient. The difference in the simulated average particle outlet velocities with 1×10^6 and 4×10^6 elements was only 1%. Figure 6 shows the results of a FLUENT simulation of particle flow (280 μm particle diameter) when released from a 9.53 mm slot aperture. It should be noted that a 46 cm narrow chute extending from the discharge slot into the receiver was not included in the FLUENT models.

4.2 Particle Velocity Measurements. The velocity distribution of particles falling through the discharge plates was measured using a high-speed camera (Allied Vision Technologies NX4-S1) with images recorded every 1/200th s with an exposure time of 250–350 μs. Rather than using particle image velocimetry, which requires lasers or high-powered lights, we analyzed visible features in successive images of the falling particle curtain. The movement of the features was tracked, and the distance the features moved in subsequent images was then divided by the time between images to obtain the velocity at various locations of the particle curtain. Several locations near the top, middle, and bottom of the particle curtain were evaluated, and at least three features were tracked at each location to quantify the uncertainty in the measurements.

Figure 7 shows three successive images of the falling particles for the 9.53 mm slot aperture. The letters (A, B, C, and D) denote the relative locations of the features that were tracked, which are outlined as oval shapes in Fig. 7. A spatial reference scale that was visible in each image was used to track the distance traveled. The number ("1") refers to the set of features that was tracked in these images. Additional sets of features were tracked in these and other images.

The measured, simulated, and analytically modeled particle velocities as a function of distance from release are plotted in Fig. 8. Results show that the measured and simulated particle velocities align closely with the analytical predictions of a single falling particle assuming no drag (see Eq. (3)) for the first couple meters. Analytical predictions of a single falling particle (280 μm) with drag yielded velocities (terminal velocity = 1.88 m/s) that

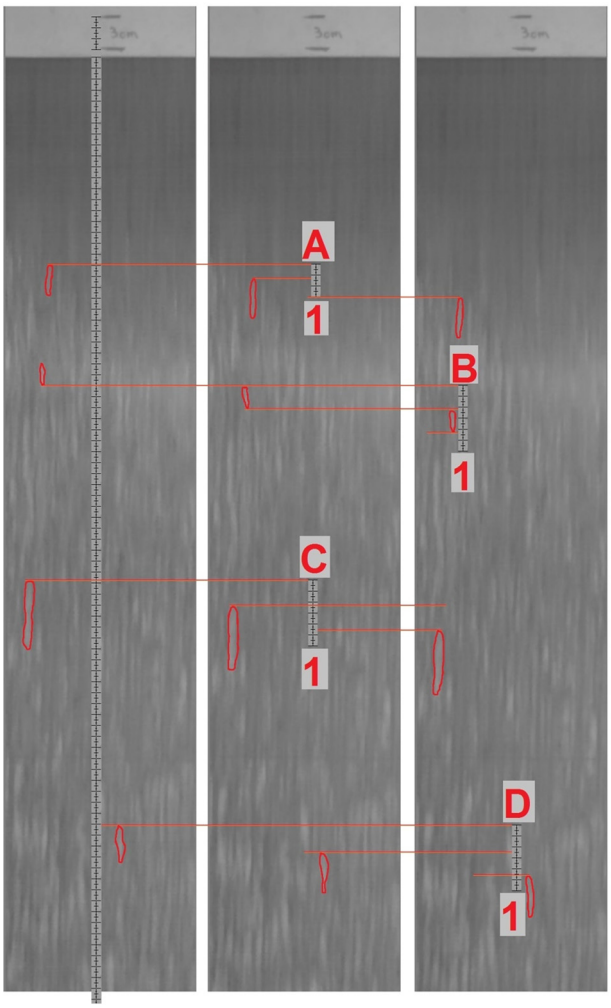

Fig. 7 Successive high-speed images of the falling particle curtain (280 μm median particle size) with a 9.53 mm (3/8 in.) slot aperture used to determine particle velocities. Each image was taken 1/200 s apart.

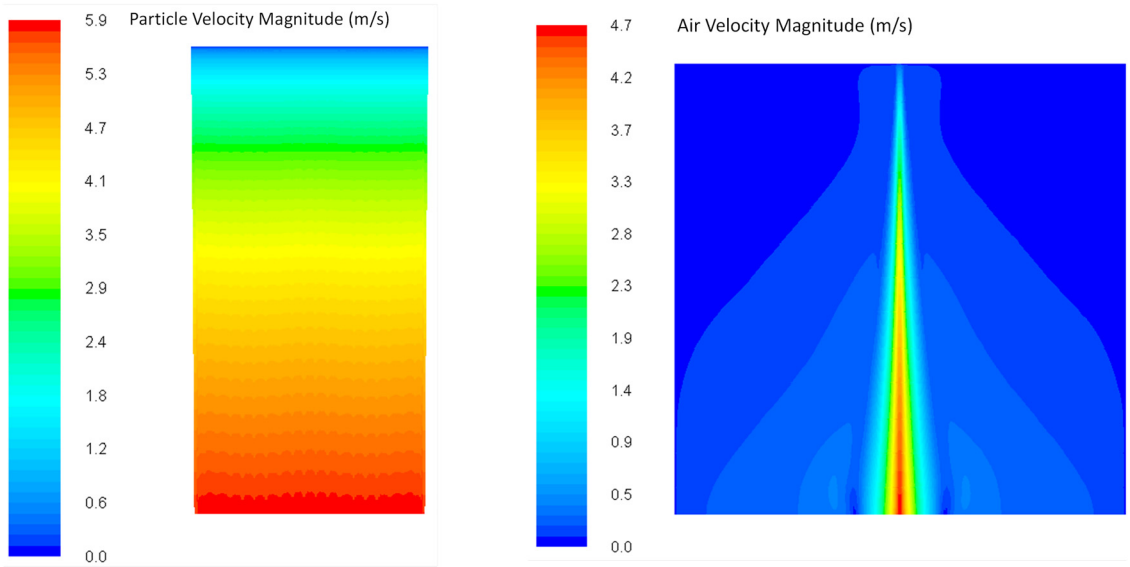

Fig. 6 ANSYS FLUENT simulation of the falling particle-curtain velocity with a 9.53 mm (3/8 in.) slot aperture. Left: front view of particle traces colored by velocity magnitude. Right: side view of entrained air velocity.

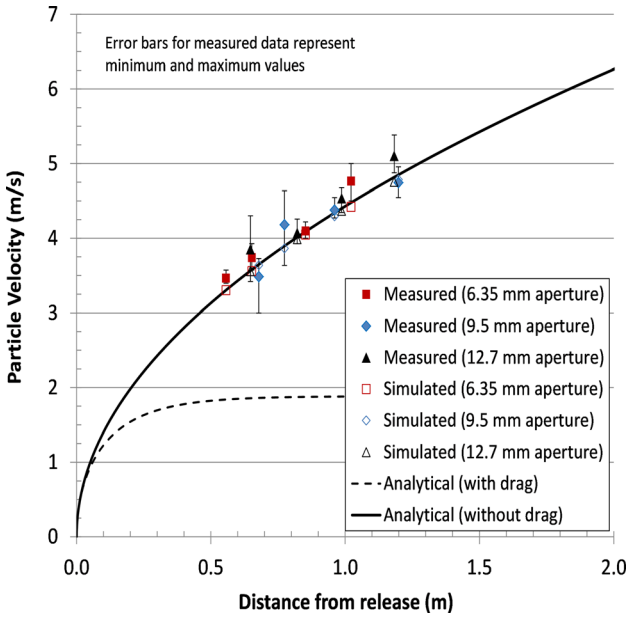

Fig. 8 Measured, simulated (ANSYS FLUENT), and analytically modeled particle velocities

were substantially lower than the measured and simulated velocities. The reason for the discrepancy is the downward entrainment of air by the large number of particles falling as a curtain through the receiver. The resulting downward bulk flow of air minimizes the air resistance on individual particles. As the particles continue to fall and accelerate, additional dispersion will occur, which will cause particles to encounter more air resistance and lower velocities relative to the analytical prediction with no drag.

5 Particle-Curtain Properties

5.1 Particle-Curtain Thickness and Width. The measured and simulated width of the particle curtain for the 6.35, 9.53, and 11.1 mm slot apertures was nearly constant at 1.2 m (see Figs. 4 and 6). The mass flow rate through the 12.7 mm slot aperture exceeded the maximum mass flow rate of the Olds Elevator, so a uniform particle release across the entire width of the discharge slot could not be obtained. The thickness of the particle curtain generally increased with distance from the release point. Figure 9 shows three side-view images of the particle curtain discharged from three different slot aperture sizes. A white poster board with length scales was placed within the particle curtain to better visualize the curtain thickness associated with a short section of the particle curtain. The board also reduced the effects from parallax and waviness along the particle curtain.

Figure 10 shows the measured and simulated particle-curtain thickness for three different slot apertures as a function of distance from release. The simulated results show that the curtain thickness actually decreases from the point of release to ~1–2 m, but then increases with increasing drop distances. This could be due to the Bernoulli principle, in which the increasing velocities of the falling particles reduce the air pressure near the center of the particle curtain, which pulls air in from outside the curtain and may push the particles together. This was observed in the FLUENT simulations. As the particles continue to fall, particle collisions may cause the particles to spread and offset the Bernoulli effect.

The measured particle-curtain thicknesses ranged from ~1–3 cm over the length of the receiver (1–2 m) and are larger than the simulated thicknesses for the different slot apertures. We postulate that this may be caused by a couple factors. First, the particles that fall through the discharge slot can have some horizontal momentum as the particles move downward and sideways

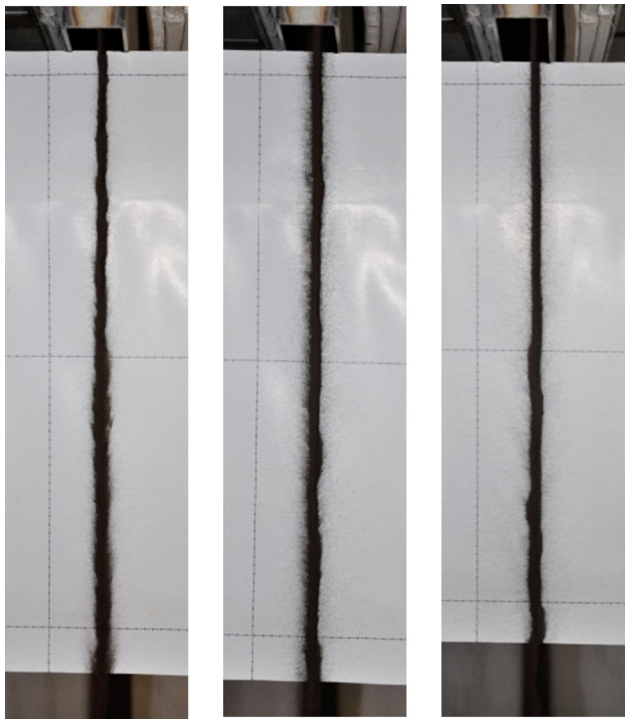

Fig. 9 Side view of particle-curtain thicknesses for 280 μm particles falling through three different slot apertures: 6.35 mm (left), 9.53 mm (middle), and 11.1 mm (right). Hash marks are 1 cm apart.

within the accumulated pile toward the slot. The simulations assumed that the particles were released from rest. The initial horizontal momentum would cause additional spreading and increased particle-curtain thickness. Preliminary modeling using the discrete element method (DEM) to account for particle–particle interactions shows improved agreement. Second, the presence of the bottom hopper caused the entrained downward air flow to be redirected upward when the particles reached the bottom hopper. This upward flow of air may have caused additional disruptions in the air flow near the curtain, which increased the curtain thickness. The bottom hopper was not included in the simulations.

Another interesting observation in Figs. 9 and 10 is that the measured particle-curtain thickness near the bottom is greatest for

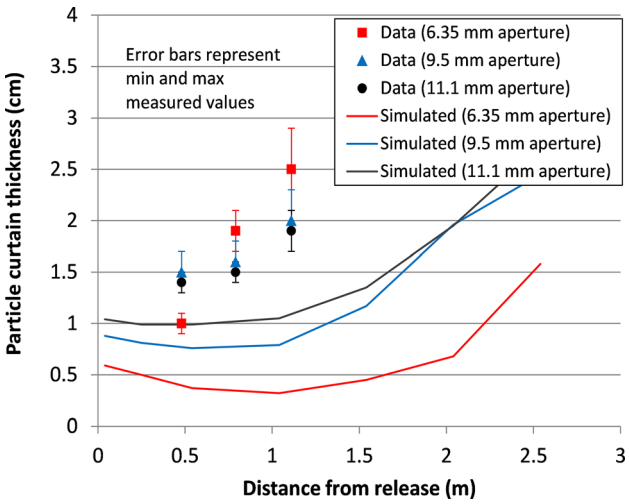

Fig. 10 Measured and simulated particle-curtain thickness as a function of drop distance

the smallest slot aperture. The widening of the particle curtain for smaller particle mass flow rates is postulated to be caused by greater dispersion of particles by the air. At lower mass flow rates, less air is entrained by the falling particles. At higher particle mass flow rates, more air is entrained downward, which would tend to pull the particles toward the center of the particle curtain (Bernoulli effect).

5.2 Falling Particle Volume Fraction. The particle bulk density (particle mass per total bulk volume) in the falling particle curtain, $\rho_{b,f}$, can be calculated as a function of drop distance, y, from the definition of the mass flow rate

$$\rho_{b,f}(y) = \frac{\dot{m}}{v(y)A(y)} \tag{7}$$

The mass flow rate, $\dot{m}$ (kg/s), for the 280 μm particles was obtained from the measurements described in Sec. 3.2.2. Equation (3) was used to analytically express the velocity as a function of drop distance, since the simulations and data showed good agreement to the analytical model (assuming no drag) for all slot apertures. The cross-sectional area of the particle curtain, $A(y)$, was calculated as the product of the width and thickness of the curtain described in Sec. 5.1.

The particle volume fraction (ratio of particle volume to total volume) within the falling particle curtain is calculated by dividing the particle bulk density of the curtain defined in Eq. (7) by the particle density (3300 kg/m^3). The measured and simulated particle volume fractions for different slot apertures are shown in Fig. 11. The initial particle volume fraction can be calculated as the particle packed-bed density (2000 kg/m^3) divided by the particle density, which yields ~0.6 or 60%. As the particles fall, the particle volume fraction decreases rapidly. The particle volume fraction decreases to less than 10% at drop distances greater than ~0.5 m from the release point due to the rapidly increasing velocity, which spreads out the particles in the vertical direction. The cross-sectional area also changes with increasing distance, although the change is relatively small within the drop distances spanned by the receiver in this study (~1–2 m). The measured particle volume fractions are lower than the simulated values due to the larger measured curtain thicknesses shown in Fig. 10 and as discussed in Sec. 5.1.

5.3 Particle-Curtain Transmittance/Opacity. The transmittance of the particle curtain is defined as the fraction of light incident on the curtain that passes through the particle curtain. The opacity of the particle curtain, defined as the ratio of incident light intercepted by the particles to the total amount of light incident on the curtain, can be calculated as one minus the transmittance. The transmittance was measured in two different ways. First, a lux meter (LX1330B) was placed both behind and in front of the particle curtain, facing toward a fixed light source, along three vertical locations of the curtain. The ratio of the lux readings gave the light transmittance through the curtain. Second, photographs were taken with and without the particle curtain present in ambient backlighting. The ratio of the pixel values in the two images with and without the particle curtain also gave the light transmittance. The advantage of this second method is that it provides a continuous measurement of the transmittance (and opacity) throughout the entire field of view. Figure 12 shows sample images using the photographic method with a Nikon D90 (f/4.5, 1/125 s). A longer exposure time was required for the images used in the opacity calculations relative to the particle velocity images (which were front lit) because of the limited amount of backlighting available. As a result, the particles in Fig. 12 appear as streaks rather than discrete particles. It is uncertain as to how this may affect the opacity calculations.

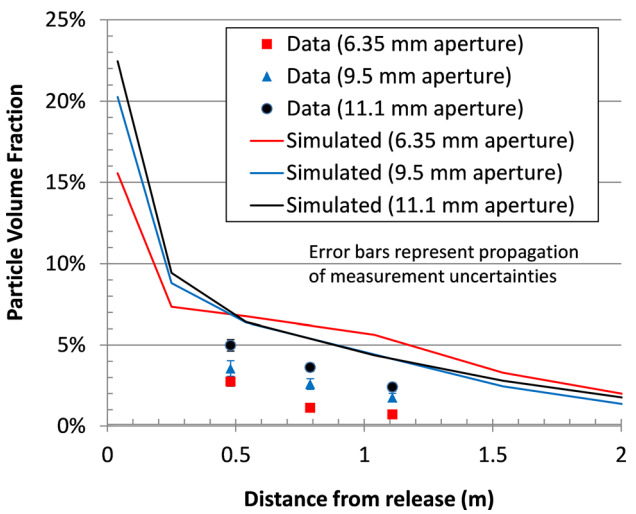

Fig. 11 Measured and simulated particle volume fraction as a function of drop distance for different slot apertures and a median particle size of 280 μm

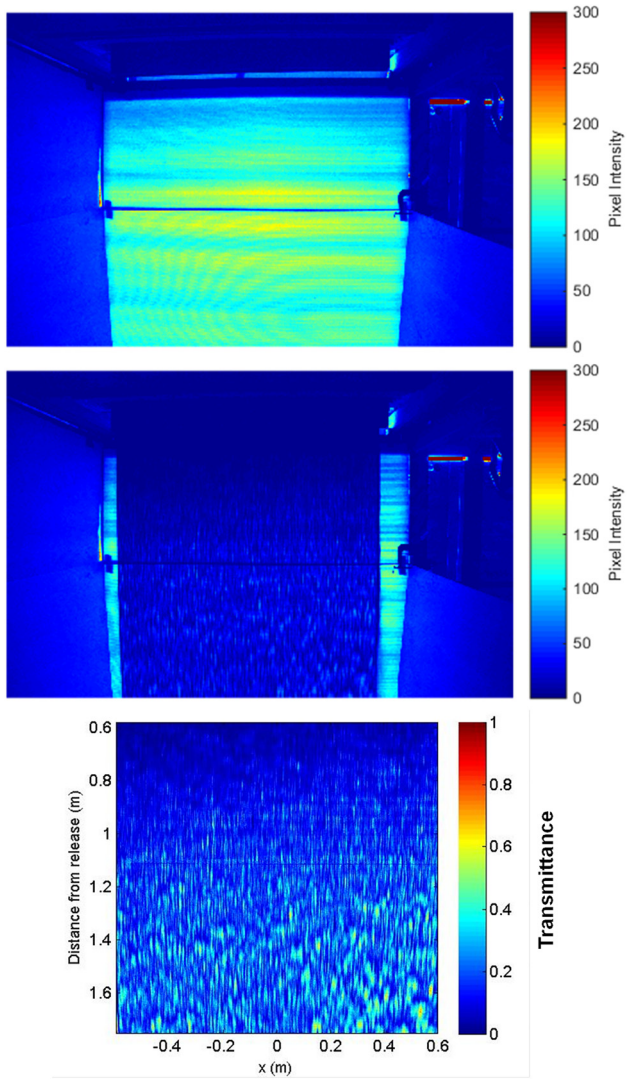

Fig. 12 Top: raw image without particle curtain. Middle: raw image with particle curtain (9.53 mm aperture, 280 μm particles). Bottom: ratio of images with and without particle curtain yielding transmittance (one minus opacity), cropped over the particle curtain.

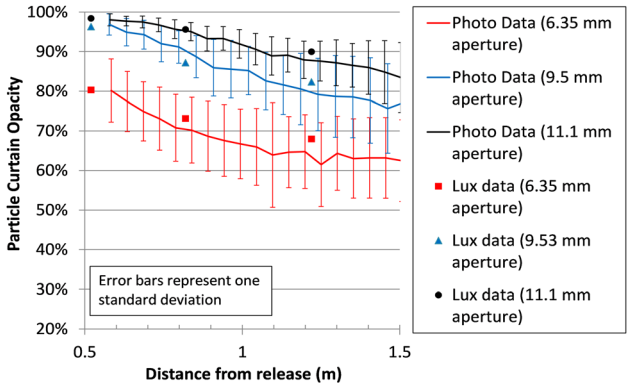

Fig. 13 Measured particle-curtain opacity (one minus transmittance) as a function of drop distance for different slot apertures and 280 μm particles

Figure 13 shows the measured opacity as a function of drop distance for three different slot apertures using both measurement methods. The measured values began at a distance of ~0.5 m from the release point, since a ~46 cm discharge chute extended from the discharge plate into the receiver. In the photographic method, the opacity was averaged along each row of pixels in the particle-curtain image corresponding to different distances from the release point, and error bars were plotted to represent one standard deviation in the measured opacity along each transect. The opacity of the particle curtain is quite high for all three slot apertures near the release point. For the 9.53 mm and 11.1 mm slot apertures, the opacity of the particle curtain is above 95% within ~0.7 m of the release point. For the 6.35 mm aperture, the opacity is ~80% within ~0.6 m of the release point. The opacity decreases with increasing distance as the particles spread apart with increasing velocity and curtain thickness.

6 Conclusions

A particle flow characterization study has been performed on ceramic particles for a prototype falling particle receiver. These studies and results will help to inform models and on-sun heating tests of falling particle receivers for concentrating solar power applications. The following conclusions can be drawn from this study:

6.1 Particle Mass Flow Rates.

- The particle mass flow rate increases with increasing slot aperture sizes according to a power law.
- Smaller particles yield a greater mass flow rate than larger particles for a given aperture size.
- The measured mass flow rates for two particle sizes were matched well with predictions from a modified Beverloo equation (see Sec. 3.2.1).
- The mass flow rate of the Olds Elevator exhibited a linear correlation ($R^2 = 0.99$) with the drive frequency. The maximum mass flow rate of the Olds Elevator exceeded the mass flow rate through the 6.35, 9.53, and 11.1 mm slot apertures, but it could not exceed the flow rate through the 12.7 mm slot aperture.

6.2 Particle Velocities

- The measured and simulated particle velocities within the first 2 m of drop distance were predicted by the analytical free-fall model assuming no drag. Particle entrainment of air reduced the drag. At longer drop distances, particle dispersion and drag are likely to increase, reducing the particle acceleration.

6.3 Particle-Curtain Properties.

- The particle-curtain width remained nearly constant along the drop length of the receiver.
- The particle thickness varied with drop distance.
  - Simulated curtain thicknesses exhibited a minimum ~1 m from the release point, perhaps from the Bernoulli effect.
  - Measured curtain thicknesses were generally larger than the simulated values due to initial horizontal momentum of the particles at the release point and an updraft of air caused by the bottom hopper.
- The particle volume fraction in the curtain decreased rapidly from a theoretical value of 60% at the release point to less than 10% within 0.5 m of drop distance.
- The particle-curtain opacity was greater than 95% within ~0.7 m of the release point for the 9.53 and 11.1 mm slot apertures and decreased steadily with increasing distance. The particle-curtain opacity was ~80% within ~0.6 m of the release point for the 6.35 mm slot aperture.

Acknowledgment

This work was funded by the DOE SunShot program under contract DE-FOA-0000595 Project 1558. The authors acknowledge Daniel Ray, J. J. Kelton, Doug Robb, Eric Coker, Andrea Ambrosini, and James Yuan for their assistance with the particle characterization tests. Sandia National Laboratories is a multi-program laboratory managed and operated by Sandia Corporation, a wholly owned subsidiary of Lockheed Martin Corporation, for the U.S. Department of Energy's National Nuclear Security Administration under Contract No. DE-AC04-94AL85000. The United States Government retains and the publisher, by accepting the article for publication, acknowledges that the United States Government retains a non-exclusive, paid-up, irrevocable, world-wide license to publish or reproduce the published form of this manuscript, or allow others to do so, for United States Government purposes.

References

[1] Ho, C., Christian, J., Gill, D., Moya, A., Jeter, S., Abdel-Khalik, S., Sadowski, D., Siegel, N., Al-Ansary, H., Amsbeck, L., Gobereit, B., and Buck, R., 2014, "Technology Advancements for Next Generation Falling Particle Receivers," Energy Procedia, **49**, pp. 398–407.
[2] Bradshaw, R. W., and Meeker, D. E., 1990, "High-Temperature Stability of Ternary Nitrate Molten-Salts for Solar Thermal-Energy Systems," Sol. Energy Mater., **21**(1), pp. 51–60.
[3] Siegel, N. P., Ho, C. K., Khalsa, S. S., and Kolb, G. J., 2010, "Development and Evaluation of a Prototype Solid Particle Receiver: On-Sun Testing and Model Validation," ASME J. Sol. Energy Eng., **132**(2), p. 021008.
[4] Tan, T. D., and Chen, Y. T., 2010, "Review of Study on Solid Particle Solar Receivers," Renewable Sustainable Energy Rev., **14**(1), pp. 265–276.
[5] Wu, W., Trebing, D., Amsbeck, L., Buck, R., and Pitz-Paal, R., 2015, "Prototype Testing of a Centrifugal Particle Receiver for High-Temperature Concentrating Solar Applications," ASME J. Sol. Energy Eng., **137**(4), p. 041011.
[6] Wu, W., Uhlig, R., Buck, R., and Pitz-Paal, R., 2015, "Numerical Simulation of a Centrifugal Particle Receiver for High-Temperature Concentrating Solar Applications," Numer. Heat Transfer, Part A, **68**(2), pp. 133–149.
[7] Flamant, G., Gauthier, D., Benoit, H., Sans, J. L., Boissiere, B., Ansart, R., and Hemati, M., 2014, "A New Heat Transfer Fluid for Concentrating Solar Systems: Particle Flow in Tubes," Energy Procedia, **49**, pp. 617–626.
[8] Flamant, G., Gauthier, D., Benoit, H., Sans, J. L., Garcia, R., Boissiere, B., Ansart, R., and Hemati, M., 2013, "Dense Suspension of Solid Particles as a New Heat Transfer Fluid for Concentrated Solar Thermal Plants: On-Sun Proof of Concept," Chem. Eng. Sci., **102**, pp. 567–576.
[9] Ma, Z. W., Glatzmaier, G., and Mehos, M., 2014, "Fluidized Bed Technology for Concentrating Solar Power With Thermal Energy Storage," ASME J. Sol. Energy Eng., **136**(3), p. 031014.
[10] Gobereit, B., Amsbeck, L., and Buck, R., 2013, "Operation Strategies for Falling Particle Receivers," ASME Paper No. ES2015-49354.
[11] Christian, J. M., and Ho, C. K., 2013, "Alternative Designs of a High Efficiency, North-Facing, Solid Particle Receiver," Energia Procedia, **49**, pp. 314–323.
[12] Khalsa, S. S. S., Christian, J. M., Kolb, G. J., Röger, M., Amsbeck, L., Ho, C. K., Siegel, N. P., and Moya, A. C., 2011, "CFD Simulation and Performance Analaysis of Alternative Designs for High-Temperature Solid Particle Receivers," ASME Paper No. ES2011-54430.

[13] Röger, M., Amsbeck, L., Gobereit, B., and Buck, R., 2011, "Face-Down Solid Particle Receiver Using Recirculation," ASME J. Sol. Energy Eng., **133**(3), p. 031009.
[14] Ho, C. K., Christian, J. M., Moya, A. C., Taylor, J., Ray, D., and Kelton, J., 2014, "Experimental and Numerical Studies of Air Curtains for Falling Particle Receivers," ASME Paper No. ES-FuelCell2014-6632.
[15] Siegel, N., Kolb, G., Kim, K., Rangaswamy, V., and Moujaes, S., 2007, "Solid Particle Receiver Flow Characterization Studies," ASME Paper No. ES2007-36118.
[16] Ho, C. K., Khalsa, S. S., and Siegel, N. P., 2009, "Modeling On-Sun Tests of a Prototype Solid Particle Receiver for Concentrating Solar Power Processes and Storage," ASME Paper No. ES2009-90035.
[17] Ho, C. K., 2016, "A Review of High-Temperature Particle Receivers for Concentrating Solar Power," Appl. Therm. Eng., **109**, pp. 958–969.
[18] Ho, C. K., Christian, J. M., Yellowhair, J., Armijo, K., and Jeter, S., 2016, "Performance Evaluation of a High-Temperature Falling Particle Receiver," ASME Paper No. ES2016-59238.
[19] Ho, C. K., Christian, J. M., Yellowhair, J., Siegel, N., Jeter, S., Golob, M., Abdel-Khalik, S. I., Nguyen, C., and Al-Ansary, H., 2015, "On Sun Testing of an Advanced Falling Particle Receiver System," SolarPACES, Cape Town, South Africa, Oct. 13–16, p. 030022.
[20] Hruby, J. M., Steeper, R. R., Evans, G. H., and Crowe, C. T., 1986, "An Experimental and Numerical Study of Flow and Convective Heat Transfer in a Freely Falling Curtain of Particles," Sandia National Laboratories, Livermore, CA, Report No. SAND86-8714.
[21] Kim, K., Moujaes, S. F., and Kolb, G. J., 2010, "Experimental and Simulation Study on Wind Affecting Particle Flow in a Solar Receiver," Sol. Energy, **84**(2), pp. 263–270.
[22] Tan, T. D., Chen, Y. T., Chen, Z. Q., Siegel, N., and Kolb, G. J., 2009, "Wind Effect on the Performance of Solid Particle Solar Receivers With and Without the Protection of an Aerowindow," Sol. Energy, **83**(10), pp. 1815–1827.
[23] Ho, C. K., and Christian, J. M., 2013, "Evaluation of Air Recirculation for Falling Particle Receivers," ASME Paper No. ES-FuelCell2013-18236.
[24] Kim, K., Siegel, N., Kolb, G., Rangaswamy, V., and Moujaes, S. F., 2009, "A Study of Solid Particle Flow Characterization in Solar Particle Receiver," Sol. Energy, **83**(10), pp. 1784–1793.
[25] Siegel, N., Gross, M., Ho, C., Phan, T., and Yuan, J., 2014, "Physical Properties of Solid Particle Thermal Energy Storage Media for Concentrating Solar Power Applications," Energy Procedia, **49**, pp. 1015–1023.
[26] Siegel, N. P., Gross, M. D., and Coury, R., 2015, "The Development of Direct Absorption and Storage Media for Falling Particle Solar Central Receivers," ASME J. Sol. Energy Eng., **137**(4), p. 041003.
[27] Knott, R., Sadowski, D. L., Jeter, S. M., Abdel-Khalik, S. I., Al-Ansary, H. A., and El-Leathy, A., 2014, "High Temperature Durability of Solid Particles for Use in Particle Heating Concentrator Solar Power Systems," ASME Paper No. ES-FuelCell2014-6586.
[28] Knott, R., Sadowski, D. L., Jeter, S. M., Abdel-Khalik, S. I., Al-Ansary, H. A., and El-Leathy, A., 2014, "Sintering of Solid Particulates Under Elevated Temperature and Pressure in Large Storage Bins for Thermal Energy Storage," ASME Paper No. ES-FuelCell2014-6588.
[29] Beverloo, W. A., Leniger, H. A., and Vandevelde, J., 1961, "The Flow of Granular Solids Through Orifices," Chem. Eng. Sci., **15**(3–4), pp. 260–269.
[30] Fowler, R. T., and Glastonbury, J. R., 1959, "The Flow of Granular Solids Through Orifices," Chem. Eng. Sci., **10**(3), pp. 150–156.
[31] Janda, A., Zuriguel, I., and Maza, D., 2012, "Flow Rate of Particles Through Apertures Obtained From Self-Similar Density and Velocity Profiles (Vol 108, 248001, 2012)," Phys. Rev. Lett., **109**(18), p. 189901.
[32] Harmens, A., 1963, "Flow of Granular Material Through Horizontal Apertures," Chem. Eng. Sci., **18**(5), pp. 297–306.
[33] Morsi, S. A., and Alexande, A. J., 1972, "Investigation of Particle Trajectories in 2-Phase Flow Systems," J. Fluid Mech., **55**(2), pp. 193–208.
[34] ANSYS, 2013, "ANSYS FLUENT Theory Guide Release 15.0," ANSYS, Canonsburg, PA.